geosciences

MDPI

Article

# Storm-Induced Boulder Displacements: Inferences from Field Surveys and Hydrodynamic Equations

**Marco Delle Rose [1,*], Corrado Fidelibus [2], Paolo Martano [1] and Luca Orlanducci [3]**

[1] Istituto di Scienze dell'Atmosfera e del Clima, Consiglio Nazionale delle Ricerche, 73100 Lecce, Italy; p.martano@isac.cnr.it
[2] Dipartimento di Ingegneria dell'Innovazione, Università del Salento, 73100 Lecce, Italy; corrado.fidelibus@unisalento.it
[3] Geopro, Geological Prospections, 73100 Lecce, Italy; lucaorlanducci@libero.it
* Correspondence: m.dellerose@le.isac.cnr.it

Received: 29 August 2020; Accepted: 17 September 2020; Published: 19 September 2020


**Abstract:** The storm of 12–13 November 2019 provoked the displacements of boulders on a central Mediterranean rocky coast; with reference to a selected area, prone to boulder production and geomorphologically monitored for years, a field-oriented study approach was applied for the phenomenon, by collating data concerning the pre-storm locations and kinematics of these boulders. The number of displaced boulders is 11, that is in terms of the morphological imprint of a specific storm, one of the major study cases for the Mediterranean. In addition, based on widely used hydrodynamic equations, the minimum wave height required to displace the boulders is assessed. The values conform with the expected values for the wave climate dominating during the causative meteorological event and give a measure of the energy of the storm slamming the coast. Boulder dislodgement usually plays a key role in determining the rate of the coastal recession, likely also in the investigated area. In view of an adverse climate evolution with a possible increase of the energy and frequency of severe storms, the results deriving from the study of this morphodynamics should be considered for hazard assessment and coastal management.

**Keywords:** wave impact assessment; characteristic wave height; Salento Peninsula; Taranto Gulf; Mediterranean Sea; November 2019 storm

## 1. Introduction

For the hazard assessment and defense planning of coastlines, reliable data on the impact produced by high-energy waves are required [1,2]. Geological surveys aimed at recognizing such an impact are indispensable in order to acquire data concerning the nearshore [3,4]. Studies of displacement modes and trajectories of boulders based on comparison among pre- and post-event data are of relevance. However, the number of cases documented in the literature is small, the initial positions of the boulders being generally unknown (see, e.g., [5,6]). Some relevant cases regard the Mediterranean coast [7–9]. The studies of these cases are illuminating in view of the prediction of boulder displacements during future storms [10,11].

In the Mediterranean Sea, throughout the second half of the 20th Century, moderate storm events prevailed, with peaks of the frequency of cyclones in winter. In the middle of the 1970s, the wind activity shifted from a decreasing trend to an increasing one [12,13]. Since the beginning of the new century, the increased occurrence of cyclones with tropical-like characteristics (i.e., medicanes) in the area has raised concerns. On 26 September 2006, a medicane battered the western coast of the Salento Peninsula (southern Italy, central Mediterranean Sea) [14]. A minimum sea level pressure of 986 hPa was registered; it was the lowest in the records of the minimal pressure during similar storms

in the whole Mediterranean area [15]. Later, several intense storms hit the Mediterranean, causing widespread damages [16–18]. Thus, future modifications of the cyclones are of concern due to the large damage potential [19,20]. As a consequence of global warming, it is predicted that at the end of the century, the cyclones will last longer and bring stronger winds [21].

In the last few years, the western coast of the Salento Peninsula has been affected by more and more severe coastal storms, and many infrastructures have been damaged. Large waves have caused dislodgement of rock boulders and breakwater blocks and damage of promenade walls [22]. The 29 October 2018 storm event [17,18] affected also the western coast of the Salento Peninsula, where it caused the displacement of some boulders [23]. One year later, on 12–13 November, a severe storm (hereinafter called IonicS19) hit the area again with considerable effects. The survey of these effects is the focus of this note. Specifically, the following is reported: (1) a description of the geomorphological imprints on the coast; (2) the inference of the hydrodynamic features of the storm; (3) useful general remarks for the coastal hazard and management issues. The note is structured as a follows: in Section 2, the features of the investigated coastal stretch are reported; in Section 3, IonicS19 is described; in Section 4, the results of the field surveys are shown; in Section 5, an assessment of the wave impact on the coast during the storm event is presented; in Section 6, the discussion and conclusion are given; finally, in Appendix A.1, some specific features of the geomorphological monitoring of the affected area are reported; and in Appendix A.2, several details of the pre- and post-storm data are explained.

## 2. Study Area

The Salento Peninsula belongs to the Apulian Platform, a crustal domain characterized by a horst-and-graben structure and formed by Cretaceous limestones overlain by Tertiary and Quaternary clastic carbonates and clayey marls. Due to the prevalence of calcareous rocks, the landscape frequently shows karst features. As a whole, the peninsula is a flat plateau gently dipping from southeast (mean altitude 100 m a.s.l.) to northwest (mean altitude 35 m a.s.l.). Throughout the Middle-Late Pleistocene, the coastal zones were morphed by the interaction between tectonic and eustatic processes [24], resulting in a staircase of marine terraces. The area herein selected for the survey faces the semi-enclosed Taranto Gulf (Figure 1). It has a microtidal regime and is moderately urbanized, crowded in summer due to tourism. A breakwater of a small harbor and an abandoned mussel breeding farm constitute the only structures along the coastline. Hundreds of boulders constitute a prominent geomorphological feature of the area; they are isolated or arranged in groups and scattered on the platform by a catastrophic event, likely a tsunami that occurred in 1456 [25]. Sand ridges on the rocky platform may be other signatures of high-energy waves, and Reference [26] traced their origin to a tsunami that occurred in 1836.

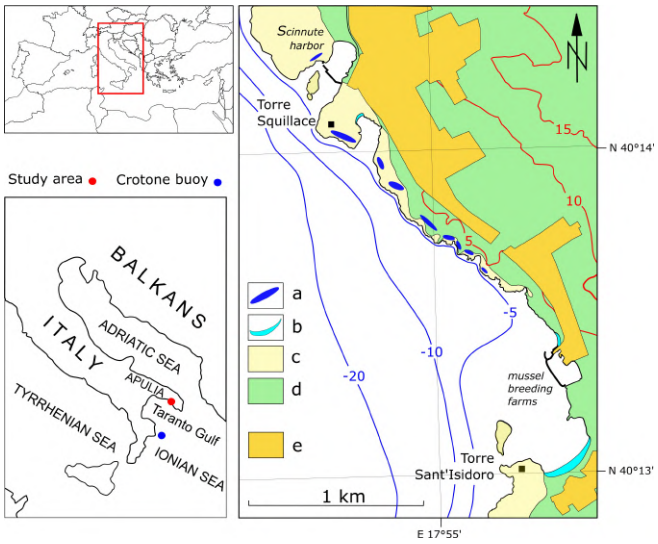


**Figure 1.** Geological map of the study area (modified from [27]); legend: a, boulder field; b, sandy beach; c, Pleistocene calcarenites; d, Cretaceous limestones; e, urban area; contour lines (red) from the technical map of Lecce Province (1:5000); isobaths (blue) from the nautical chart of Istituto Idrografico della Marina Militare (1:100,000).

The coastal area is generally flat; major slopes are close to the coastline, especially between −5 m and 5 m a.s.l. The slope of the shoreface, between the isobaths −5 and −20 m, ranges from 1.5 to 6%. The rocky substratum is generally covered by sands settled by benthic communities. Among Torre Squillace and Torre Sant'Isidoro, the cliff is 5 m high, almost entirely below the sea level, and is interrupted by sandy beaches (Figure 1). A coastal platform, hundreds of meters large, extends inland from the edge of the cliff. On the platform, the paraconcordant contact between Cretaceous limestones and a late Quaternary calcarenitic terrace is visible [28]. These rocks are carved by typical coastal karst forms such as pinnacles and solution pans. More recent continental deposits (lithified eluvium, carbonate breccia) frequently cover the previous formations. Enhanced karst processes, due to brackish groundwater flowing to the sea, cause the formation of collapse dolines and control the morphological evolution of the coastline [29].

Some of the boulders scattered along the surveyed area were possibly moved by storm waves during the last 50–100 years; such a hypothesis is being tested [27]. Moreover, for the peculiar geological features, the site is prone to boulder production, as evidenced by field observations. Therefore, since 2017, the stretch of the rocky coast between Torre Squillace and Torre Sant'Isidoro (Figure 1) is subjected to geomorphological monitoring with a focus on the locations of the boulders (see Appendix A.1). After IonicS19 (see Section 3), the displacements of eleven boulders were defined through a field survey and photographic documentation (see Section 4).

As far as the wave climate is concerned, since 1989, a reference for the Taranto Gulf is the Crotone buoy (Figure 1). It belongs to the Italian ondametric network and is placed offshore (mooring depth 80 m) at the southwestern side of the semi-enclosed basin. By analyzing the data of the buoy, the derived value of $H_s$, the maximum significant wave for a 50 year return period, is 6.3 m [30]. Estimates of $H_s$ for a 100 year return period, resulting from additional processing of the buoy data, are 7.5 and 8.2 m, obtained by using an ECMWF model and a NOAA model, respectively [31].

## 3. The 11/12-13/2019 Storm

### *3.1. Synoptic Conditions*

For the meteorological overview of the storm, the archive maps of the model cascade GLOBO-BOLAM-MOLOCH of the Institute of Atmospheric Sciences and Climate, National Research

Council of Italy (CNR-ISAC) are used [32,33]. Since the first days of the month, a stable configuration of high pressure conditions over the middle Atlantic and the Caspian Sea regions favored the formation of an extended trough at 500 hPa going from North-Central Europe down to the Mediterranean Sea, bringing frequent and quite strong southern winds over the Salento Peninsula. On 5 November, a storm with winds blowing at about 12 m/s and at a 10 m height offshore impinged on the western Salento coast followed on the 9th by another storm with southwestern winds of about 10 m/s. On 11 November, a trough at 500 hPa approaching from the northwest of France deepened strongly over the Gulf of Lyon, an area that often acts as a feeding area, increasing the strength of Mediterranean storms in this period of the year. The trough then migrated southward in the Tyrrhenian Sea, reaching Sicily after acquiring more strength turning around the Atlas plateau and thus conveying very strong winds over the Taranto Gulf (Figure 2a). IonicS19 was characterized by a deep surface pressure minimum developed over the Tyrrhenian Sea. This caused the development of a secondary minimum on the other side of Italy on the northern Adriatic Sea (Figure 2b). This minimum migrated towards the Venice Lagoon, and the consequent veering wind among the lagoon boundaries caused a very anomalous surge on different parts of the lagoon, with a height often well over 1.5 m, one of the highest of the last few decades [34]. In the meantime, some forecast models predicted the evolution of the storm into a medicane [35]. A strong southeastern wind over the Salento Peninsula started soon after midnight from the southeast and persisted for about 12 h from the same direction with an offshore fetch of about 800 km, down to the Libyan coast (Figure 3). In the following evening, the wind turned S-SW until the afternoon of 13 November, with the fetch reduced to about 350 km, further reducing until the end.

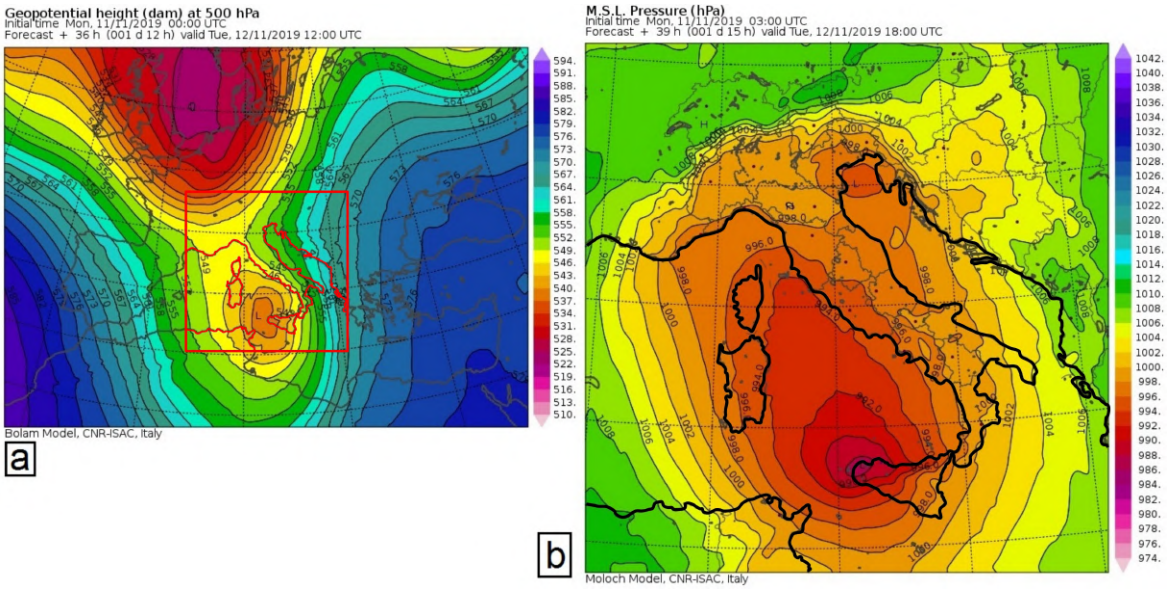


**Figure 2.** (**a**) Geopotential height at 500 hPa over the western Mediterranean Sea at 12.00 UTC on 12 November 2019; (**b**) surface pressure over the central Mediterranean at 18.00 UTC on 12 November 2019. Notice also the secondary minimum over the northern Adriatic. Images downloaded from [32]; the coastline is marked.

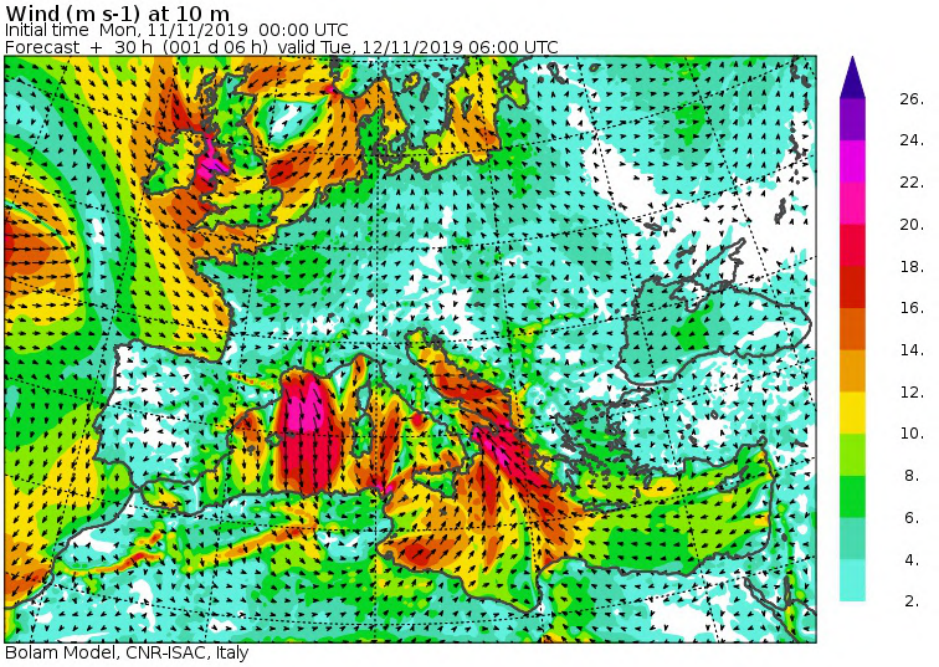


**Figure 3.** Wind speed at a 10 m height on 12 November 2019 at 6.00 UTC; note the quite long fetch down to the Libyan coast; image downloaded from [32].

### *3.2. Meteorological Data and Wave Modeling*

Two datasets are used to describe the wave climate and the wind features. They come from the following stations (Figure 4): the Porto Cesareo wind gauge, a reference station of the Italian Civil Protection Department (local identification codex: A02TLE; elevation 12 m a.s.l.) [36]; the S. Maria di Leuca station, pertaining to the meteorological service of the Italian Air Force and the reference station of the World Meteorological Organization (WMO code: 16,360; ICAOcode: LIBY; elevation 112 m a.s.l.) [37]. The wind speed and direction recorded hourly by the A02TLE wind gauge from 11 November to 14 November are reported in Figure 5. For comparison, the semi-diurnal wind speed and direction recorded hourly by the LIBY station are reported in Figure 6.

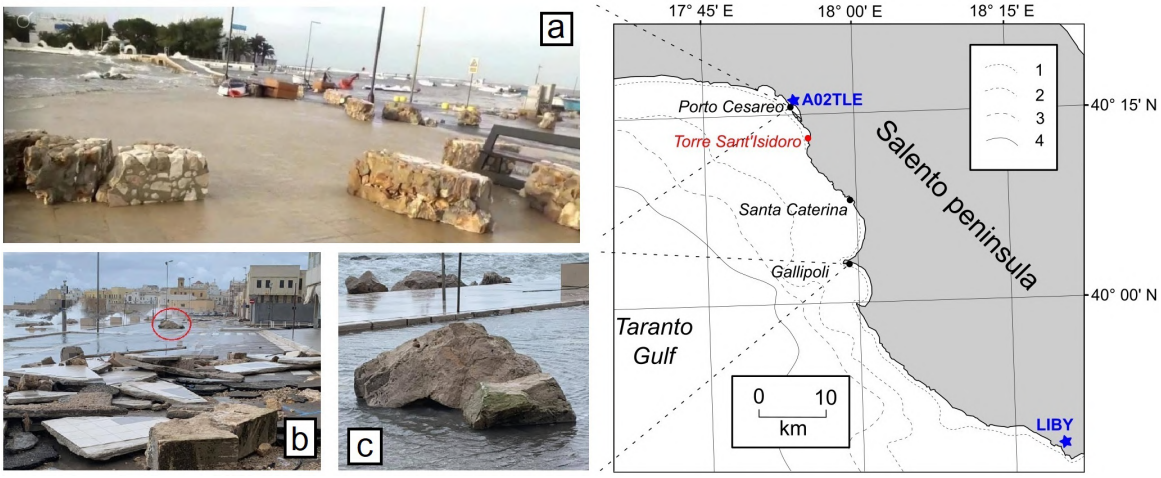


**Figure 4.** Examples of damages caused by the 12–13 November 2019 storm to some urban areas; (**a**) Porto Cesareo, blocks of a destroyed promenade wall; (**b**) Gallipoli, blocks of promenade wall and pavement, the red circle marks the largest breakwater block displaced during the storm; (**c**) close view of the block.

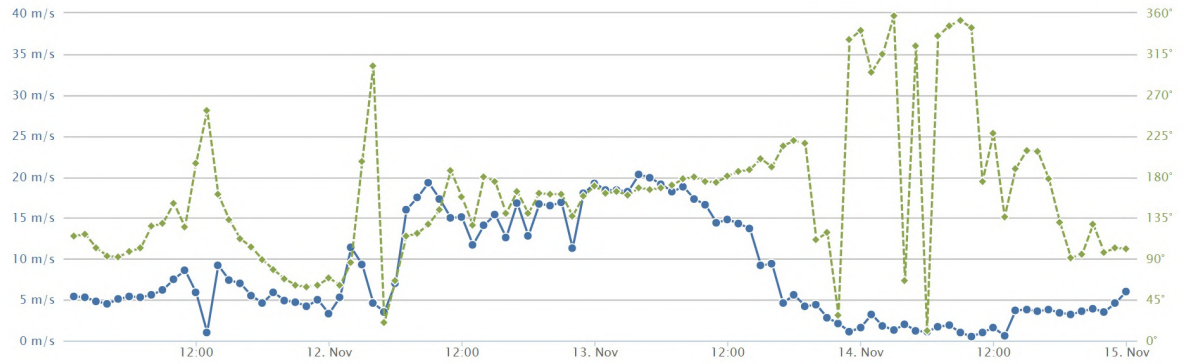


**Figure 5.** Wind speed and direction (dashed line) recorded hourly by the A02TLE wind gauge; image downloaded 16 May 2020, from the SIMOP site of the Apulian Basin Authority (AdBP) [36].

From Figure 5, the veering of the wind direction during 13 November is apparent. Because of the position of the anemometer, the wind speed is a good proxy for the 10 m height wind speed over the sea, while, with reference to Figure 6, the increased wind speed is due to the height of the LIBY station (112 m a.s.l.).

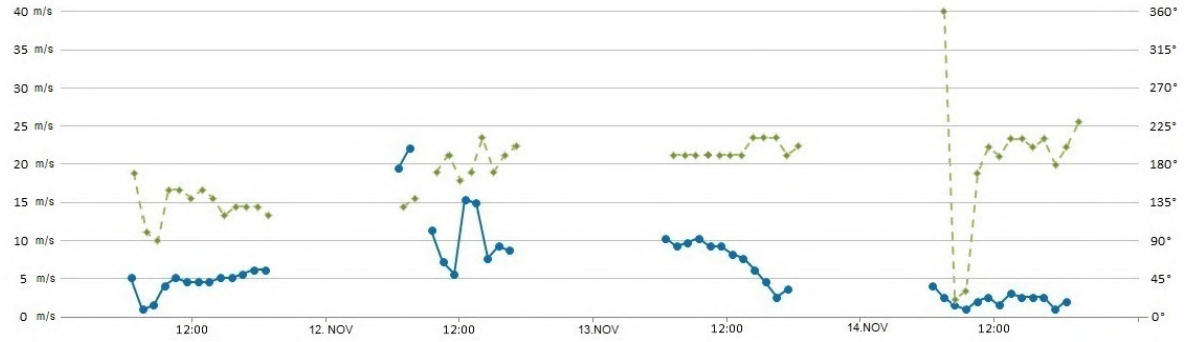


**Figure 6.** Wind speed and direction (dashed line) recorded hourly by the LIBY station; image drawn using the data downloaded 11 December 2019, from the OGIMET site [37].

The coastal meteorological stations of the Italian Air Force service, in addition to the wind vectors, also provide semi-diurnal measurements of the sea state (i.e., sea conditions) and swell wave lengths $S_l$ [38]. These parameters are quantified by means of the aeronautical Q-signals QUK and QUL, respectively, and are correlated with both the Douglas Sea Scale and the Beaufort Wind Force Scale.

The QUK and QUL values, measured by the LIBY station before, during, and after IonicS19, are reported in Table 1. From these values, one can infer that the storm intensity grew during the night of 11 November; thus, in the early morning of 12 November, a peak of nine for QUK was measured, corresponding to an estimate of more than 14 m for $H_s$. In the meantime, the swell length exceeded 200 m (very high $S_l$ description). The storm, as recorded by the LIBY station, gradually lost strength on 13 November. The large estimates of $H_s$ (>14 m and 9–14 m) in Table 1 seem overestimated, compared to the value of $H_{m0}$ (7–9 m) calculated by means of Equation (2). However, the QUK data come from "experienced observers"' estimation of the 30% highest waves during direct observation of the sea surface.

The following equations were used to obtain estimates of the wave period $T$ and the characteristic wave height $H_{m0}$. They relate $T$ and $H_{m0}$ at the wave spectral peak to the wind speed at 10 m height offshore $U$ and to the fetch over the sea $F$ [39] ($g$ is gravity):

$$gT/U = 0.2857(gF/U^2)^{1/3} \quad (1)$$

$$gH_{m0}/U^2 = 0.0016(gF/U^2)^{1/2} \quad (2)$$

The obtained values of $T$ and $H_{m0}$ are 14–15 s and 7–9 m, respectively, with a fetch of 800 km and a wind speed between 15 and 20 m/s. It must be noted that the characteristic wave height $H_{m0}$ is nearly equivalent to the significant wave height $H_s$ [40,41].

**Table 1.** QUK and QUL signals recorded hourly by the LIBY station in November 2019; data downloaded 11 December 2019 from the OGIMET site [37] (UTC time).

| Day/Hours | QUK | $H_s$(m) | QUL | $S_l$ Description |
|---|---|---|---|---|
| 11/14.00–16.00 | 3 | 0.5–1.25 | 2 | low |
| 11–12/17.00–05.00 | no data | - | no data | - |
| 12/06.00–13.00 | 9 | >14 | 8 | very high |
| 12/15.00–16.00 | 8 | 9–14 | 7 | high |
| 12–13/17.00–05.00 | no data | - | no data | - |
| 13/06.00–12.00 | 8 | 9–14 | 7 | high |
| 13/13.00–14.00 | 7 | 6–9 | 6 | rough |
| 13/15.00–16.00 | 5 | 2.5–4 | 3 | light |
| 13–14/17.00–05.00 | no data | - | no data | - |
| 14/06.00–07.00 | 2 | 0.1–0.5 | 1 | very low |

### 3.3. Storm Impact

IonicS19 caused a number of damages on structures along a 30 km stretch of coast. The most affected places were the city of Gallipoli and the villages of Santa Caterina and Porto Cesareo (Figure 4). Promenade walls were destroyed and breakwater blocks displaced towards the coastal road. In Gallipoli, several boats sunk, and numerous infrastructures along the seafront were destroyed. The largest breakwater block has an estimated volume of 3 $m^3$ and weighs 8 t (Figure 4). In addition, as previously mentioned, on the shore platform between Torre Squillace and Torre Sant'Isidoro (Figure 1), eleven boulders were dislodged (see Section 4).

## 4. Data of the Field Surveys

The displacements of the eleven boulders caused by IonicS19 were identified by means of: (1) a recognition of the detached surfaces (the so-called "sockets" [42]); (2) a comparison of transect photos taken before and after the storm, respectively; (3) marks of the displacements on the joints previously bounding the boulders. The locations of the investigated boulders are shown in Figure 7. They are all placed in the central sector of the investigated area, inside the splash-spray zone; the relative locations are reported in Table 2, together with pre-storm locations.

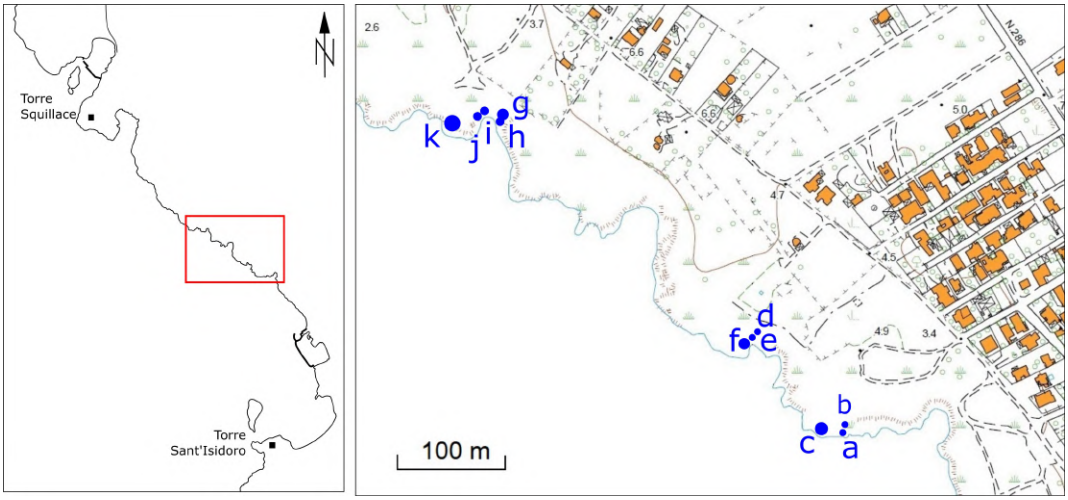


**Figure 7.** Locations of the boulders displaced by the 12–13 November 2019 storm. Topography from the technical map of the Lecce Province (1:5000).

**Table 2.** Pre- and post-geographical coordinates of the displaced boulders; ind., indeterminable.

| | Pre-Storm Location | | Post-Storm Location | |
|---|---|---|---|---|
| **Boulder ID** | **Latitude** | **Longitude** | **Latitude** | **Longitude** |
| SI19a | 40°13′34.09″ N | 17°55′17.79″ E | ind. | ind. |
| SI19b | 40°13′34.25″ N | 17°55′17.83″ E | 40°13′34.22″ N | 17°55′17.82″ E |
| SI19c | 40°13′34.20″ N | 17°55′17.51″ E | ind. | ind. |
| SI19d | 40°13′37.03″ N | 17°55′14.06″ E | 40°13′37.20″ N | 17°55′14.28″ E |
| SI19e | 40°13′36.97″ N | 17°55′14.01″ E | 40°13′37.05″ N | 17°55′14.16″ E |
| SI19f | 40°13′37.03″ N | 17°55′14.06″ E | 40°13′37.04″ N | 17°55′14.07″ E |
| SI19g | 40°13′43.82″ N | 17°55′05.10″ E | 40°13′43.89″ N | 17°55′05.12″ E |
| SI19h | 40°13′43.81″ N | 17°55′05.09″ E | ind. | ind. |
| SI19i | 40°13′44.07″ N | 17°55′04.60″ E | ind. | ind. |
| SI19j | 40°13′44.05″ N | 17°55′04.59″ E | 40°13′44.21″ N | 17°55′04.72″ E |
| SI19k | 40°13′43.81″ N | 17°55′02.97″ E | 40°13′43.81″ N | 17°55′02.97″ E |

The post-storm locations of SI19a, SI19c, SI19h, and SI19i were not recognized. The lengths $a$, $b$, and $c$ of the axes of each boulder (assumed prismatic) are reported in Table 3, together with the distances $x$ and $x_f$ from the cliff edge, respectively pre-storm and post-storm. Boulder dimensions are determined according to rules defined in the literature [43].

**Table 3.** Dimensions of the boulder axes $a$, $b$, $c$ , pre-storm distances from the cliff $x$, post-storm distances from the cliff $x_f$. BT, boulder type: JB, joint-bounded; SA, sub-aerial (not joint-bounded). MT, movement type: ST, saltation; SL, sliding; OV, overturning; ind., indeterminable.

| | $a$(m) | $b$(m) | $c$(m) | $x$(m) | $x_f$(m) | BT | MT |
|---|---|---|---|---|---|---|---|
| SI19a | 0.6 | 0.6 | 0.4 | 0.5 | ind. | SA | ind. |
| SI19b | 1.6 | 1.2 | 0.3 | 8.5 | 6.5 | SA | ST |
| SI19c | 2.6 | 1.7 | 0.6 | 1.5 | ind. | SA | SL |
| SI19d | 1.3 | 1.1 | 0.4 | 12 | 19.5 | SA | ST |
| SI19e | 2.3 | 0.7 | 0.6 | 11 | 16.5 | JB | ST |
| SI19f | 2.8 | 2.4 | 0.4 | 12 | 12.5 | SA | ST |
| SI19g | 1.7 | 1.5 | 0.5 | 9 | 11.5 | SA | OV |
| SI19h | 1.1 | 0.7 | 0.4 | 8 | ind. | JB | ST |
| SI19i | 1 | 0.8 | 0.7 | 17 | ind. | SA | ind. |
| SI19j | 1,2 | 0,8 | 0,6 | 18,5 | 22 | SA | ind. |
| SI19k | 4.8 | 2.2 | 1.1 | 8.0 | 8.2 | JB | ST |

In what follows, several pieces of evidence of the boulder displacements are presented. Supplementary field data are in Appendix A.2. Boulders SI19a, SI19b, SI19c (SI19c coincides with boulder B1 of [27]) are at the southeast side of the investigated coastal stretch (Figure 7). Boulders a, b, and c (henceforth, "a", "b", etc., instead of SI19a, SI19b, etc.) were identified through inspection of the sockets; for Boulders a and c, photo comparisons confirmed the field evidence (Figure A2). Furthermore, for c, drag marks due to the sliding on the platform were identified. The trajectory ends in the sea (Figure A3). In Figure 8, the comparison between the c locations pre- and post-storm are shown.

The storm-induced displacements of Boulders d, e, and f (Figure 7) can be easily detected by considering the field evidence. Note that Boulders d and f result from the breaking of one pre-existing boulder (the pre-existing boulder was named B2 in [27]) (for details, see Figure A4). The boulder displacements can be defined also through the comparison of transect photos (Figure A5). Due to IonicS19, Boulder f underwent a short saltation (0.5 m), while Boulder d was displaced 7.5 m (Table 3). Boulder e jumped f, as indicated by the detachment niche (i.e., socket), the marks over f's surface, and e's final position (Figure 9).

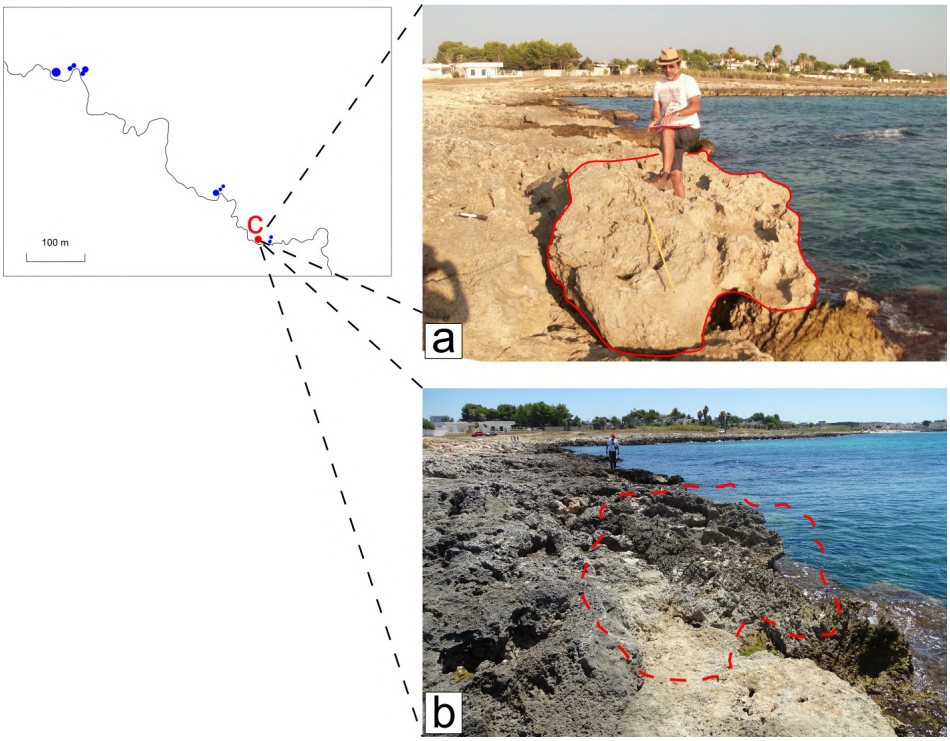


**Figure 8.** Pre- and post-storm event states: (**a**) photo taken before the storm; Boulder c is marked by the continuous line; (**b**) photo taken after the storm; the pre-storm position is marked by the dashed line.

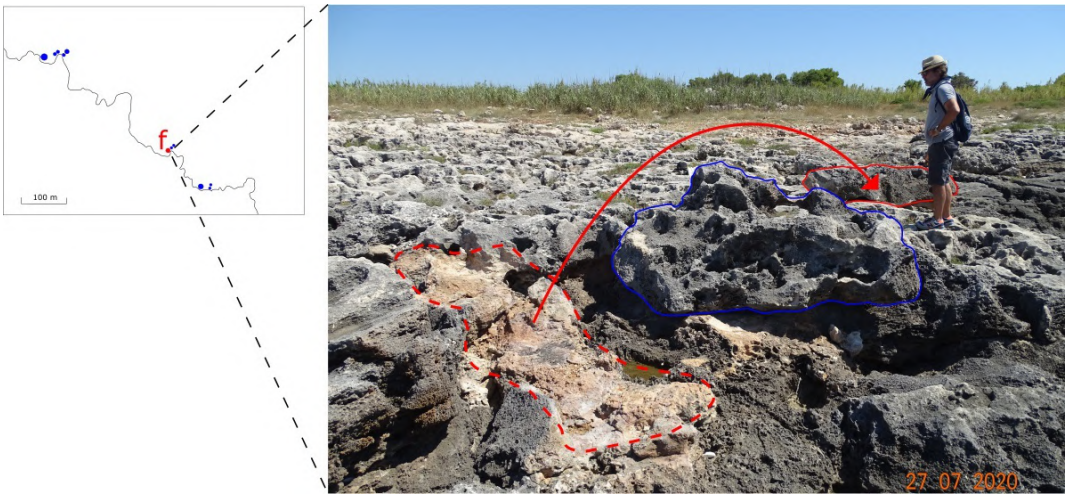


**Figure 9.** The saltation movement of Boulder e; the socket (red dashed) and the final position (red solid) are shown; the blue line highlights Boulder f.

The displacements of g, h, i, j, and k (Figure 7) were kinematically different. By comparison of the transect photos (Figure A6) and by field observations, it is apparent that g overturned. Boulders h and i disappeared after the storm. Boulder j was displaced 3.5 m. Finally, Boulder k (Figure 10), the largest of the eleven boulders, underwent a short saltation (Table 3). Failures on the rock surfaces for the high disruptive stresses caused several rock wedges to be detached from the bedrock and the boulder. This feature was decisive for the recognition of k (Figure A7).


**Figure 10.** Photo of Boulder k taken parallel to the $b \times c$ plane; the arrows indicate the shear failures on the rocky surfaces.

## 5. Hydrodynamics Equations

To alternatively quantify the impact of the storm, hydrodynamic equations are applied to estimate the minimum energy of a solitary wave necessary for a boulder displacement. The energy is expressed in terms of (minimum) height $H_m$. According to [44], for joint-bounded and sub-aerial (non-joint-bounded) boulders transported by saltation, $H_m$ is, respectively:

$$H_m \geq \frac{2c\,(\gamma_r/\gamma_w - 1)\,(\cos\theta + \mu_s \sin\theta)}{C_L} \tag{3}$$

$$H_m \geq \frac{2c\,(\gamma_r/\gamma_w - 1)\cos\theta}{C_L} \tag{4}$$

where $\gamma_r$ and $\gamma_w$ are the unit weights of rock and water, respectively, $\mu_s$ is the coefficient of static friction along rock surfaces, $\theta$ is the bed slope angle, and $C_L$ is the lift coefficient. For sub-aerial boulders transported by sliding and by overturning, Reference [44] proposed, respectively:

$$H_m \geq \frac{2c\,(\gamma_r/\gamma_w - 1)\,(\mu_d \cos\theta + \sin\theta)}{C_D(c/b) + (\mu_s C_L)} \tag{5}$$

$$H_m \geq \frac{2c\,(\gamma_r/\gamma_w - 1)\,(\cos\theta + (c/b)\sin\theta)}{C_D\,(c^2/b^2) + C_L} \tag{6}$$

where $\mu_d$ is the coefficient of dynamic friction [45] and $C_D$ is the drag coefficient.

Alternatively, according to [46], $H_m$ for joint-bounded boulders and sub-aerial boulders is, respectively:

$$H_m \geq \frac{2V\,(\gamma_r - \gamma_w)\,(\cos\theta + \mu_s \sin\theta)}{C_L(acq)\gamma_w} \tag{7}$$

$$H_m \geq \frac{2\mu V \gamma_r}{C_D(acq)\gamma_w} \tag{8}$$

where $V$ is the boulder volume and $q$ is the boulder area coefficient.

Literature data are used herein for the choice of the values of the coefficients in Equations (3)–(8); the selected values are: $\mu_s = 0.65$, $\mu_d = 0.6$, $C_L = 0.178$, $C_D = 1.95$, $q = 0.73$ [4,8,44–47]. The bed slope angle $\theta$ is assumed to be zero due to the very flat morphology of the study area; thus, Equation (3) coincides with the Equation (5) proposed by [48], adapted for storm waves. The results are shown in Table 4.

**Table 4.** Minimum wave heights $H_m$ required to displace the boulders.

| | Nandasena et al. (2011) | Engel and May (2012) |
|---|---|---|
| SI19a | 3.59 | 0.98 |
| SI19b | 2.70 | 1.97 |
| SI19c | 0.72 | 2.79 |
| SI19d | 3.59 | 1.80 |
| SI19e | 5.39 | 8.62 |
| SI19f | 3.59 | 3.94 |
| SI19g | 2.03 | 2.46 |
| SI19h | 3.59 | 8.62 |
| SI19i | 6.29 | 1.31 |
| SI19j | 5.39 | 1.31 |
| SI19k | 9.90 | 27.10 |

## 6. Discussion and Conclusions

### *6.1. Boulder Displacements and Wave Energy*

On 12 November 2019, IonicS19 battered the western coast of the Salento Peninsula moving from SE to NW (Section 3). It severely struck the city of Gallipoli, where the most significant signature was the displacement of a breakwater block having an estimated volume of 3 $m^3$ and a weight of 8 t (Figure 4). As recorded by the A02TLE wind station, the storm reached the study area in the early morning (Figure 5). At Porto Cesareo, the wind speed did not exceed 21 m/s. However, wind persisted for about 12 h from SE with an offshore fetch of about 800 km (Figure 3). Between Torre Sant'Isidoro and Torre Squillace (Figure 1), the storm caused the displacement of eleven boulders (Section 4). Their size ranged from 0.6 × 0.6 × 0.4 $m^3$ to 4.8 × 2.2 × 1.1 $m^3$ (Table 3). For six out of eight boulders, the kinematics was saltation (for three boulders, the type of movements was not determined). The displacements were roughly normal to the coastline, except for one boulder that traveled an alongshore trajectory as shown by drag marks (Figure A3).

Probably, Boulders c and f were already moved by previous storms of the last 50–100 years [27]. If this hypothesis were confirmed, the proneness to the boulder production of the investigated stretch of coast, as inferred from field evidence, would be further proven. Especially in the central sector of the coast between Torre Squillace and Torre Sant'Isidoro, where the base of the Quaternary calcarenite crops out, the boulder production seems to be eased (Figure 7). However, the variability alongshore of the wave energy transfer should be considered. In fact, the effects of the local bathymetry may be larger than the effects of the regional-scale coastal morphology, which are in general assumed dominant. For example, Reference [49] found significant variations in wave energy transmission over short distances (about 100 m) due to the foreshore features, thus suggesting a similar scale of variation for the coastal recession rate.

As previously mentioned (Section 5), the minimum wave height $H_m$ required to displace the boulders (Table 4) may give a measure of the wave energy impact on the coast, as proposed by several authors [4,8,47]. With reference to Table 4, it is noted that the two sets of equations furnish different results. With the exception of Boulder k, $H_m$ results in always being lower than 9 m, corresponding to the maximum characteristic wave height $H_{m0}$ as estimated by Equation (2). By using Equations (3)–(6), $H_m$ values even close to 6 m are obtained, while, by using Equations (7) and (8), $H_m$ does not exceed 4 m, except for Boulders e, h, and k. However, we remark that these hydrodynamic equations have limitations. Reference [50] pointed out that, apart from flaws in the formulas, the estimation of both $C_L$ and $C_D$ is critical; therefore, instead of applying values excerpted from the literature, the estimation should be accomplished with strict reference to the local physical conditions. As an example, higher values than the one (0.178) usually used for $C_L$ were obtained by both field and modeling investigations [51,52]. Such a finding reduces the minimum energy wave required to initiate the boulder displacement (see the equations in Section 5).

Other results in Table 4 deserve comments. An impacting wave only 2 m high is required to overturn Boulder g (Equation (6)); thus, even a moderate rough sea condition was predisposing the boulder to overturn. Actually, a boulder must overcome the roughness in its vicinity to reach a position suitable to the overturning [53]. By a detailed observation of the micro-topography along the transect normal to the coast and crossing the position of Boulder g, the effect of this process on the boulder displacement may be advanced. There is a critical angle (Figure A8) that has to be exceeded for the overturning.

As far as Boulder k (the largest one) is concerned, a displacement of 0.2 m was measured during the field survey (Figures 10 and A7). As a comparison term, for the other boulders, the displacement ranged between 0.5 m and 7.5 m (computed as the difference between the final and initial position; see Table 3). By using Equation (7), the wave height required to displace Boulder k seems overestimated. Similar considerations were reported in the literature [8,47]. Instead, Equation (3) furnishes a more plausible value and suggests that deep-water waves can hit the coast with small changes in wave height. By applying the formulas to the breakwater block displaced at Gallipoli (Figure 4), the resulting $H_m$ values are: 12.13 m with both Equations (3) and (4), 2.13 m with Equation (7), and 16 m with Equation (8). Again, the equations of [44] return more plausible results, suggesting a greater impact on the Gallipoli coast than on the investigated area, as confirmed by the values of QUK recorded at the LIBY station (Table 1).

### 6.2. Next Research Goals

The above discussed questions suggest caution in making conclusions from Table 4 and push the research towards specific goals. Moreover, dealing with the equations for boulder displacements provoked by solitary waves, the strong influence of non-dimensional factors on the results, such as the ratio between the axes of the boulder in the wave plane, should be also considered [54]. On the other hand, camera monitoring of the effects produced by storms on rocky coasts suggest that the occurrence of boulder displacement is the result of the "impact of multiple small waves rather than of a singular big one" [9]. With respect to the possible actions of multiple waves, an increase of a wave height up to a factor of five may be also considered [55].

A process that supposedly contributed to the displacement of k is hydraulic fracturing as described by [56]. The wave impact on a cliff may induce intense fluid pressures in the rock discontinuities as they are filled with water during wave runup and overtopping (Figure A7b). The pressurization is repeated and may lead to failures or fatigue with consequent detachment of rock slabs, which are free to be displaced. Another process potentially involved could be the development of an overtopping bore [57–59], occurring when large waves overtop sloping beaches, coastal cliffs, or defense structures and move inland like bore flows. With reference to the concept of green water, the changes in water velocity during the impact-runup-overtopping sequence have bee investigated [60]. Aiming to identify possible research directions in boulder displacements, the finding of these authors about the relation between the wave phase speed and the maximum flow velocities of each phase of the sequence should be considered. The studies of these phenomena in relation to the production and movement of coastal boulders are increasing [61,62]. In other contributions of the authors, the processes were analyzed and quantified by resorting to specific hydrodynamic equations.

As far as the morphodynamic evolution of the studied coast is concerned, by considering that the current sea level was reached in six thousand years after the end of the last eustatic rise, the boulder displacements may have strongly contributed to the recession rate. Such displacements are nonlinear and depend on physical, chemical, and biological phenomena acting at different temporal and spatial scales. However, storms may give rise to high boulder productions in thousands of years, especially where soft rocks crop out, as in the case herein exposed [63,64].

In view of an adverse climate evolution with a corresponding increase of storm intensities and frequency, the investigated morphodynamics process must be carefully evaluated for proper hazard assessment and coastal management. The increasing risks due to the storm events seem confirmed

by the last decade of records of the LIBY station (Section 3; see Figure 4 for the location). In fact, the number of stormy days has grown in the past four years; in the same period, the energy of extreme events has also increased (Figure 11).

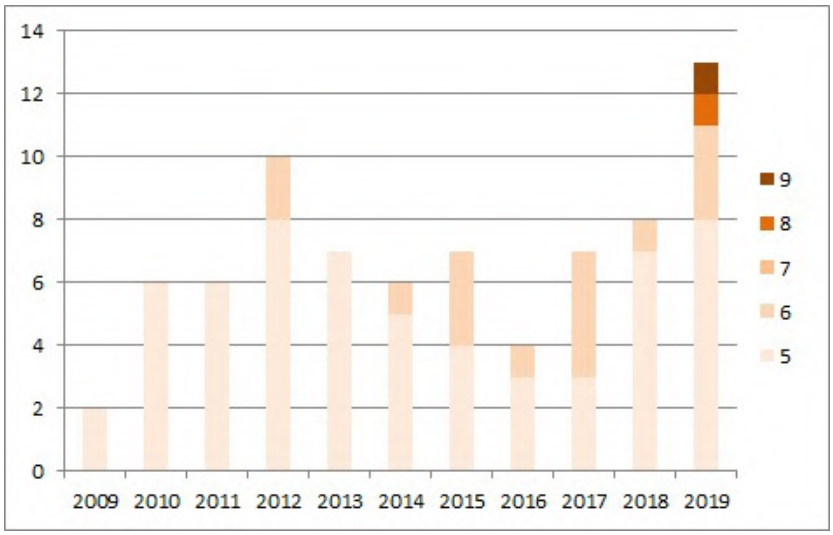


**Figure 11.** Stormy days occurring in 2009–2019 as recorded at the LIBY station. The considered thresholds are a duration of more than six hours and QUK $\geq$ 5. Image elaborated by data downloaded from the OGIMET site [37].

The stretch of coast under investigation is characterized by a high production of boulders, so the need for continuous monitoring emerges. Repeated field surveys were functional in order to verify the mobility of the boulders as a consequence of the storms. In the next few years, geomorphological monitoring will continue and will be finally supported by a GIS system.

**Author Contributions:** Conceptualization and methodology: M.D.R., C.F., P.M., and L.O.; field investigation: M.D.R. and L.O.; meteorological data curating: P.M.; writing drafts: M.D.R.; writing, review and editing: M.D.R., C.F., and P.M. All authors read and agreed to the published version of the manuscript.

**Funding:** This research received no external funding.

**Acknowledgments:** The authors wish to acknowledge L. Ciricugno (ISAC-CNR) for the assistance in the photographic survey.

**Conflicts of Interest:** The authors declare no conflict of interest.

## Appendix A

### *Appendix A.1. Geomorphological Monitoring Area*

The geomorphological surveys of the Sant'Isidoro-Torre Squillace area began in 2017. The position, the dimensions, the orientations (strike and dip) of the $a \times b$ planes, the distance from the cliff edge, and the micro-morphological features of all the boulders larger than 0.5 $m^3$ were acquired during multiple surveys. The collected data are included in a database to be linked to a GIS. Field surveys were accomplished after each storm since September 2018. The geomorphological effects of the storm of 12–13 November 2019 were right away verified. Due to the bad weather conditions and the lock-down following the COVID-19 pandemic, the post-storm survey ended in July 2020.

In Figure A1, the boulder fields of the area are mapped. They were studied with a focus on the geomorphological setting. For example, in Figure A1, a group of imbricated boulders positioned along the edge of a collapse sinkhole are shown. One of the objectives of the ongoing research is to establish the chronology of the geomorphological events that led to this arrangement.

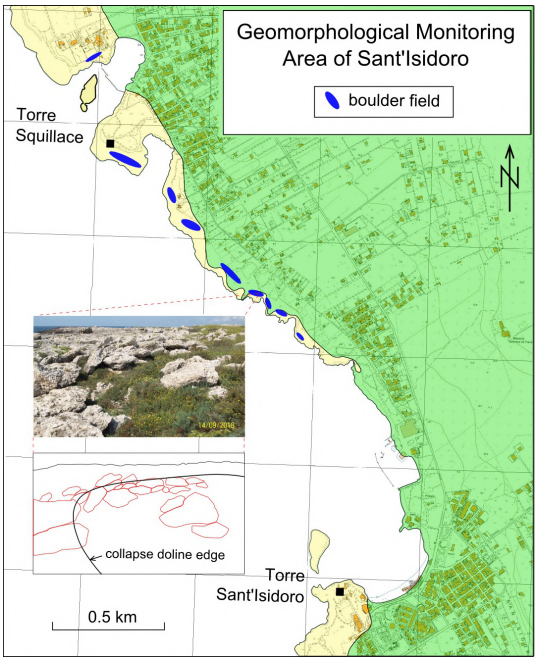


**Figure A1.** Geological map of the monitoring area with the location of the boulder fields (see Figure 1 for the legend); a group of imbricated boulders on a doline edge is clearly visible in the pictures.

A further development of the research will be the study of the sedimentological effects of the storms on pebbles and small boulders inside the bay, by means of structure-from-motion photogrammetry techniques.

*Appendix A.2. Boulder Displacement Features*

Field survey details and data supplemental to Section 4 are reported in what follows. In Figure A2, the comparison between the pre- and post-storm states of a short stretch of coast is shown. We mention the lack of Boulders a and c.

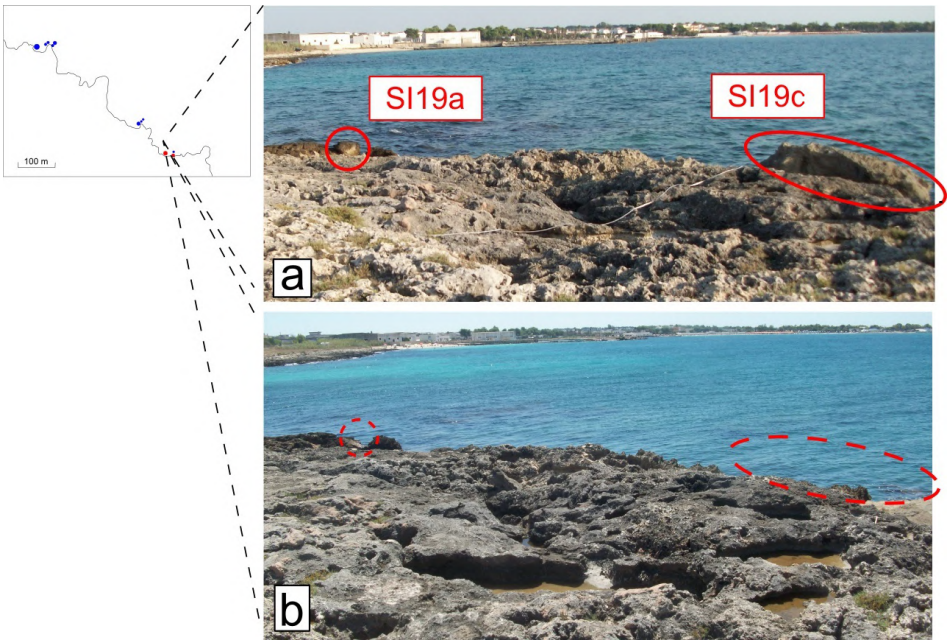


**Figure A2.** Comparison between pre- and post-storm event states; (**a**) photo taken before the storm with Boulders a and c; (**b**) photo taken after the storm; the lack of boulders is highlighted by the dashed lines.

In Figure A3, evidence of the displacements of Boulders b and c is shown. Note that Boulder c is visible in a pre-storm satellite image of Google Earth (Figure A3a). The sliding of c due to the wave impact during IonicS19 is pointed out by drag marks over the platform (Figure A3b). These marks cross the coastline; thus, the inferred trajectory of c ends in the sea (Figure A3c). Despite its small size and the proximity to the cliff edge (Table 3), Boulder b underwent a short displacement (about 2 m) (Figure A3d).

As reported above (Section 4), Boulders d and f resulted from the breaking of one pre-existing boulder (named B2 by [27]), due to IonicS19. Boulder d has a volume of just over 0.5 $m^3$, while Boulder f has a volume of 2.7 $m^3$ (Table 3). The latter was displaced 0.5 m (thus, it currently has almost the same position of B2) and is visible in the satellite images of Google Earth (Figure A4a). The fracture along which the two boulders separated is highlighted in Figure A4b, while in Figure A4c, a perspective view of Boulders d, e, and f can be observed.

In Figure A5, a comparison between the pre- and post-storm states of the zone of Boulders d, e, and f is reported. The transect photo of Figure A5a documents the post-IonicS19 state of the site. One can observe the current positions of the boulders and the sockets of Boulders e and f. The pre-IonicS19 is documented by Figure A5b,c. In the latter, the fracture causing the breaking of the boulder B2 of [27] is highlighted.

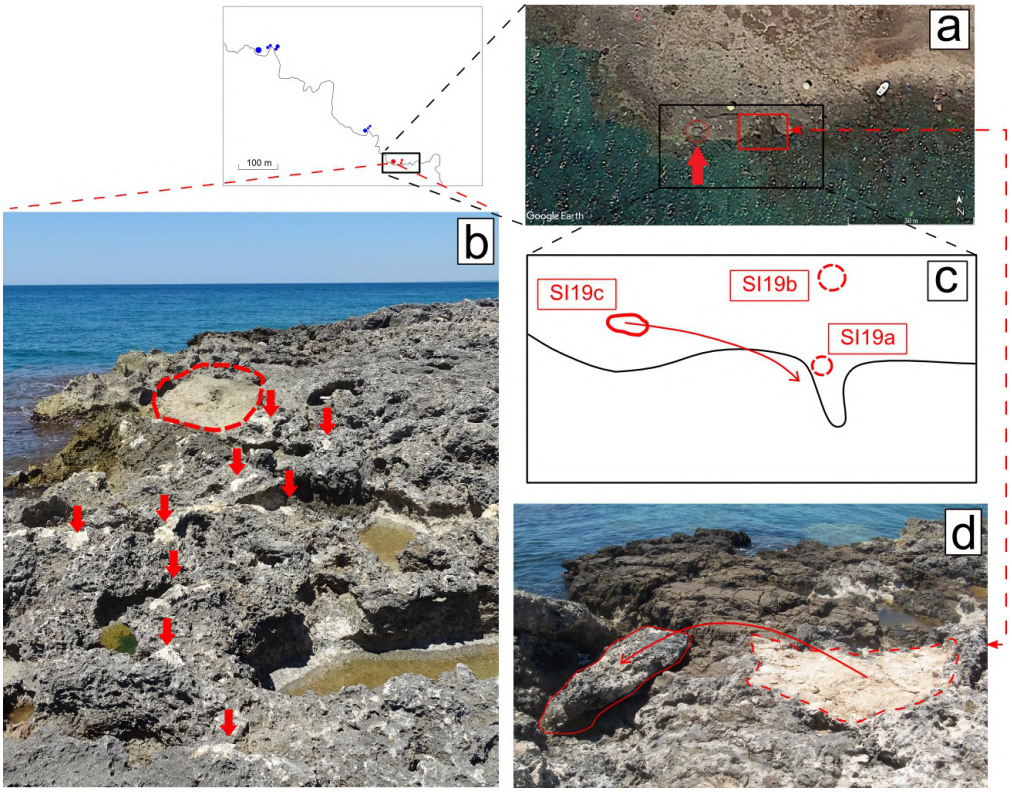


**Figure A3.** Evidence of geomorphological imprints on the surveyed area of the storm of 12–13 November 2019: (**a**) 2015 Google Earth satellite image with the location of Boulder c; (**b**) drag marks for the sliding of Boulder c (the dashed line marks the pre-storm location); (**c**) the inferred trajectory of c as defined through the field survey; (**d**) the socket and the post-storm location of Boulder b (the supposed saltation movement is also drawn).

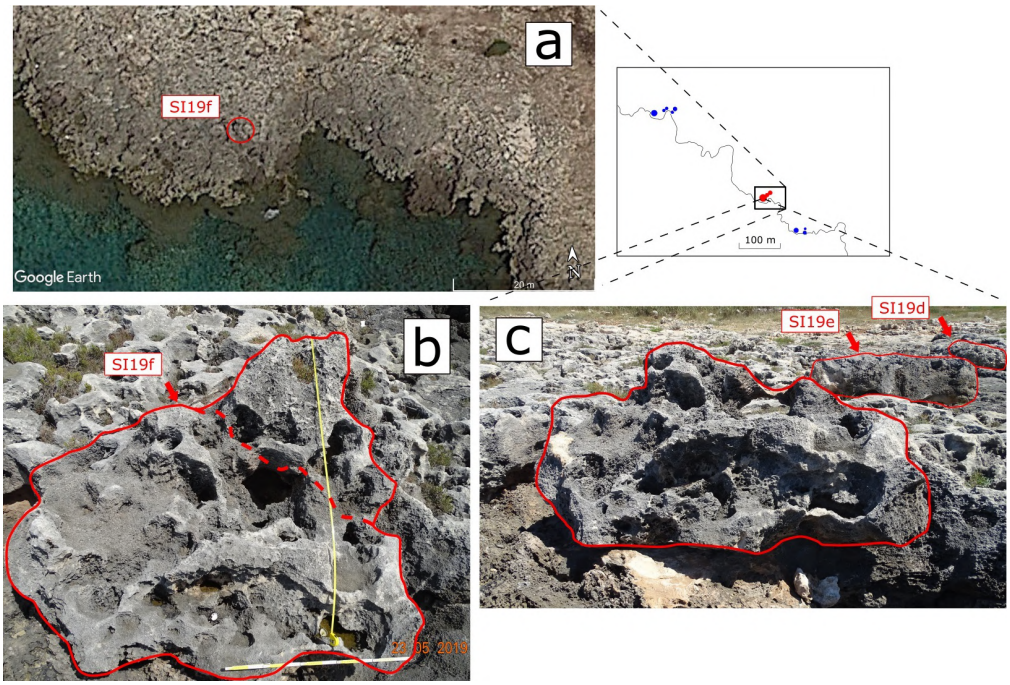


**Figure A4.** Comparison between pre- and post-storm event states: (**a**) 2015 Google Earth satellite image with the location of Boulder f; (**b**) pre-storm image of the boulder with the new fracture; (**c**) post-storm image of f (note the change of shape) with Boulders d and e in the background. The fresh unweathered rock surface under the boulder is part of the socket.

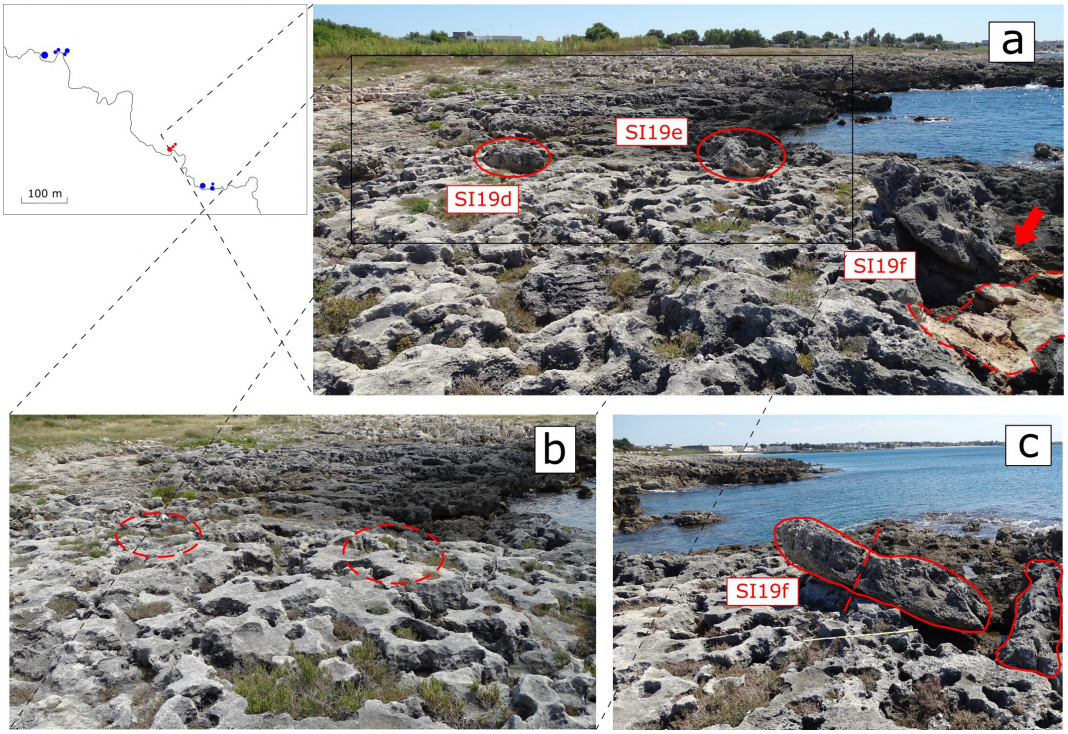


**Figure A5.** Comparison between pre- and post-storm states: (**a**) post-storm state of the zone of Boulders d, e, and f, the socket of Boulder f (red arrow), and the socket of Boulder e (dashed line); (**b**) pre-storm state (the post-storm locations of Boulders d and e are marked by dashed lines); (**c**) a pre-storm image of Boulder f with the fracture caused by the storm, the initial location (solid line) of Boulder e.

Furthermore, Boulders g and k are visible in the satellite images of Google Earth (Figure A6a). The transects of Figures A6b,c allow an easy comparison of before and after the storm event.

By observing the rock wedges detached from the bedrock, the imprint of the storm on Boulder k was detected (Section 4). The boulder was first detached from the rock mass. A fracture propagation can be advanced as the cause of the detachment. In Figure A7, an explicative sketch is shown. Presumably, two non-persistent rock mass fractures (dashed lines in the sketch) were pried open by the high water pressures generated by the wave. Regarding the geological nature of the fractures, the horizontal one is a stratification plane, while the sub-vertical one is of tectonic origin. The rock bridges of these fractures were disrupted (a tensile failure occurred), and the block was separated by the rock mass. The high pressures from the top of the sub-vertical fracture laterally pushed the wedges that slid once the shear strength on the fractures was reached. It is worth mentioning that, in case the fractures are not submerged, the water of the wave pressurizes the air inside the fractures with a sort of piston effect, with an increased damaging impact [65].

Boulders g and h, in the sub-aerial and in joint-bounded conditions, respectively (Table 3), had different fates (Section 4). Initially, one overlapped the other (Figure A8), then g was found overturned, while h was not found after the storm. There are no clues to understand if the movements took place at the same time. However, the overturning of g was possible after the exceeding of the critical angle $\theta_c$ (Section 6; Figure A8), as shown by [53].

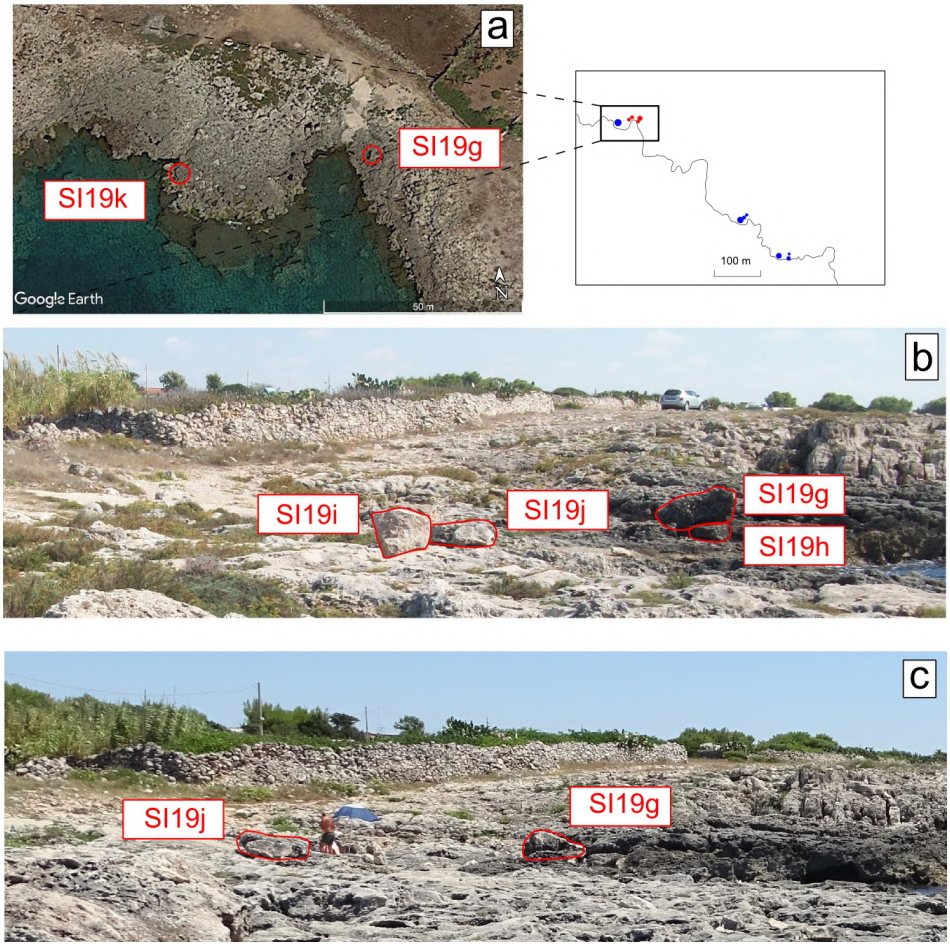


**Figure A6.** Comparison between pre- and post-storm event states: (**a**) 2015 Google Earth satellite image with the locations of the boulders; (**b**) pre-storm location of Boulders g, h, i, and j; (**c**) post-storm locations; note that Boulders h and i are missing.

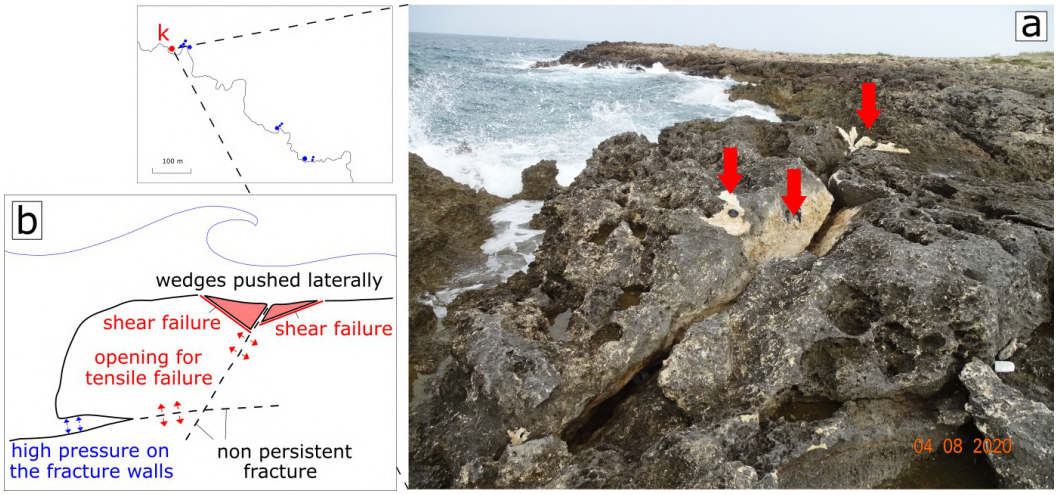


**Figure A7.** Details of the detachment surfaces of the rock wedges dislodged by Boulder k during the 12–13 November 2019 storm. (**a**) The detached surfaces indicated by arrows; (**b**) sketch of the fracturing process with the new fractures and the detached rock wedges.

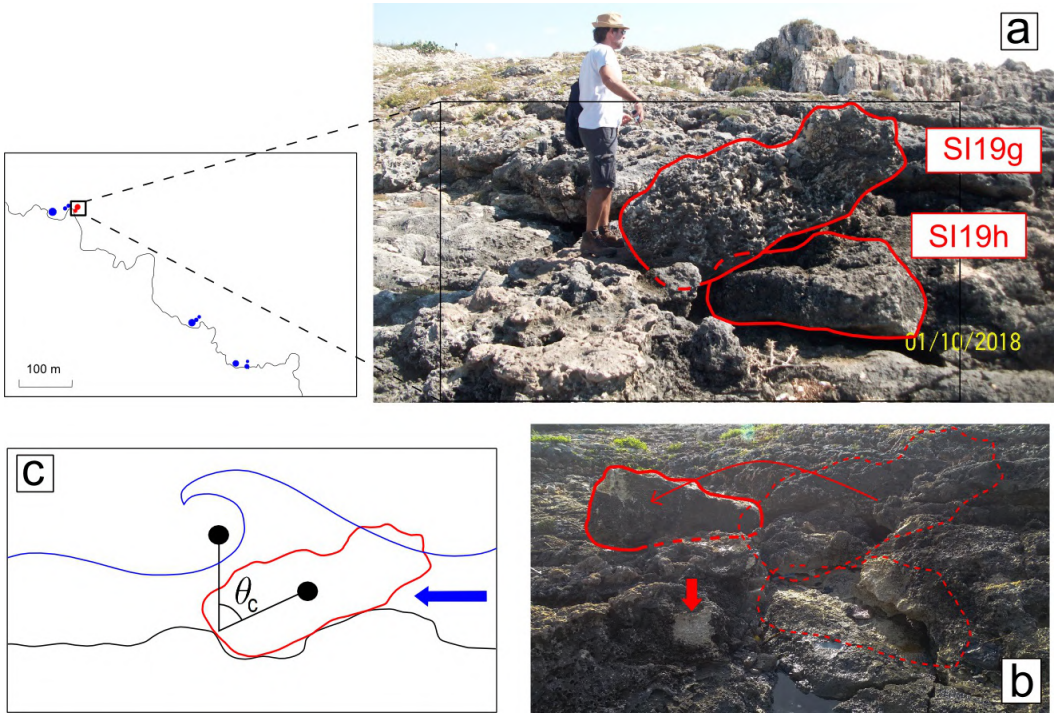


**Figure A8.** Comparison between pre- and post-storm event states: (**a**) pre-storm locations of Boulders g and h; (**b**) post-storm overturned positions of Boulder g (note the marks indicated by the arrow, probably the sign of the impact of a boulder on the bedrock); (**c**) angular threshold $\theta_c$.

## References

1. Hansom, J.D.; Switzer, A.D.; Pile, J. Extreme waves: Causes, characteristics, and impact on coastal environments and society. In *Coastal and Marine Hazards, Risks, and Disasters*; Ellis, J.T., Sherman, D.J., Eds.; Elsevier: Amsterdam, The Netherlands, 2015; pp. 307–334.
2. You, Z.J. Tropical Cyclone-Induced Hazards Caused by Storm Surges and Large Waves on the Coast of China. *Geosciences* **2019**, *9*, 131. [CrossRef]
3. Naylor, L.A.; Stephenson, W.J.; Smith, H.C.M.; Way, O.; Mendelssohn, J.; Cowley, A. Geomorphological control on boulder transport and coastal erosion before, during and after an extreme extra-tropical cyclone. *Earth Surf. Proc. Land.* **2016**, *41*, 685–700. [CrossRef]

4. Huang, S.Y.; Yen, J.Y.; Wu, B.L.; Shih, N.W. Field observations of sediment transport across the rocky coast of east Taiwan: Impacts of extreme waves on the coastal morphology by Typhoon Soudelor. *Mar. Geol.* **2020**, *421*, 106088. [CrossRef]
5. Süssmilch, C.A. Note on some recent marine erosion at Bondi. *R. Soc. N. S. W. J. Proc.* **1912**, *46*, 71–82.
6. Cox, R.; Zentner, D.B.; Kirchner, B.J.; Cook, M.S. Boulder ridges at the Aran Islands (Ireland): Recent movements caused by storm waves, not tsunamis. *J. Geol.* **2012**, *120*, 249–272. [CrossRef]
7. Mastronuzzi, G.; Sansò, P. Large boulder accumulation by extreme waves along the Adriatic coast of southern Apulia (Italy). *Quat. Int.* **2004**, *120*, 173–184. [CrossRef]
8. Piscitelli, A.; Milella, M.; Hippolyte, J.C.; Shah-Hosseini, M.; Morhange, C.; Mastronuzzi, G. Numerical approach to the study of coastal boulders: The case of Martigues, Marseille, France. *Quat. Int.* **2017**, *439*, 52–64. [CrossRef]
9. Scicchitano, G.; Scardino, G.; Tarascio, S.; Monaco, C.; Barracane, G.; Locuratolo, G.; Milella, M.; Piscitelli, A.; Mazza, G.; Mastronuzzi, G. The First Video Witness of Coastal Boulder Displacements Recorded during the Impact of Medicane "Zorbas" on Southeastern Sicily. *Water* **2020**, *12*, 1497. [CrossRef]
10. Noormets, R.; Crook, K.A.W.; Felton, E.A. Sedimentology of rocky shorelines: 3. Hydrodynamics of megaclast emplacement and transport on a shore platform, Oahu, Hawaii. *Sediment. Geol.* **2004**, *10*, 41–65. [CrossRef]
11. Goto, K.; Miyagi, K.; Kawana, T.; Takahashi, J.; Imamura, F. Emplacement and movement of boulders by known storm waves—Field evidence from the Okinawa Islands, Japan. *Mar. Geol.* **2011**, *283*, 66–78. [CrossRef]
12. Maheras, P.; Flocas, H.A.; Patrikas, I.; Anagnostopoulou, C. A 40 year objective climatology of surface cyclones in the Mediterranean region: Spatial and temporal distribution. *Int. J. Climatol.* **2001**, *21*, 109–130. [CrossRef]
13. Pirazzoli. P.A.; Tomasin, A. Recent near-surface wind changes in the central Mediterranean and Adriatic areas. *Int. J. Climatol.* **2003**, *23*, 963–973. [CrossRef]
14. Moscatello, A.; Miglietta, M.M.; Rotunno, R. Numerical Analysis of a Mediterranean "Hurricane" over Southeastern Italy. *Mon. Weather Rev.* **2008**, *136*, 4373–4397. [CrossRef]
15. Fita, L.; Romero, R.; Luque, A.; Emanuel, K.; Ramis, C. Analysis of the environments of seven Mediterranean tropical-like storms using an axisymmetric, nonhydrostatic, cloud resolving model. *Nat. Hazards Earth Syst. Sci.* **2007**, *7*, 41–56. [CrossRef]
16. Amores, A.; Marcos, M.; Carrió, D.S; Gómez-Pujol, L. Coastal impacts of Storm Gloria (January 2020) over the north-western Mediterranean. *Nat. Hazards Earth Sys. Sci.* **2020**, *7*, 1955–1968. [CrossRef]
17. Cavaleri, L.; Bajo, M.; Barbariol, F.; Bastianini, M.; Benetazzo, A.; Bertotti, L.; Chiggiato, J.; Davolio S.; Ferrarin, C.; Magnusson, L.; et al. The October 29, 2018 storm in Northern Italy—An exceptional event and its modeling. *Prog. Oceanogr.* **2019**, *178*, 102178. [CrossRef]
18. Ferrarin, C.; Valentini, A.; Vodopivec, M.; Klaric, D.; Massaro, G.; Bajo, M.; De Pascalis, F.; Fadini, A.; Ghezzo, M.; Menegon, S.; et al. Integrated sea storm management strategy: The 29 October 2018 event in the Adriatic Sea. *Nat. Hazards Earth Syst. Sci.* **2020**, *20*, 73–93. [CrossRef]
19. Androulidakis, Y.S.; Kombiadou, K.D.; Makris, C.V.; Baltikas, V.N.; Krestenitis, Y.N. Storm surges in the Mediterranean Sea Variability and trends under future climatic conditions. *Dyn. Atmos. Ocean.* **2015**, *71*, 56. [CrossRef]
20. Romera, R.; Gaertner, M.A.; Sánchez, E.; Domínguez, M.; González-Alemán, J.J.; Miglietta, M.M. Climate change projections of medicanes with a large multi-model ensemble of regional climate models. *Glob. Planet. Chang.* **2017**, *151*, 134–143. [CrossRef]
21. González-Alemán, J.J.; Pascale, S.; Gutierrez-Fernandez, J.; Murakami, H.; Gaertner, M.; Vecchi, G.A. Potential Increase in Hazard From Mediterranean Hurricane Activity With Global Warming. *Geophys. Res. Lett.* **2019**, *46*, 1754–1764. [CrossRef]
22. Delle Rose, M.; Fidelibus, C.; Miglietta, M.M. Cambiamento climatico e protezione delle coste. *Ithaca Viaggio Nella Sci.* **2020**, *15*, 47–55. (In Italian)
23. Ciricugno, L.; Delle Rose, M.; Fidelibus, C.; Orlanducci, L.; Mangia, M. Sullo spostamento di massi costieri causato da onde "estreme" (costa ionica salentina). *Geol. E Territ.* **2019**, *16*, 15–23. (In Italian)
24. Doglioni, C.; Tropeano, M.; Mongelli, F.; Pieri, P. Middle-Late Pleistocene uplift of Puglia: An "anomaly" in the Apenninic foreland. *Mem. Soc. Geol. Ital.* **1996**, *51*, 101–117.

25. Mastronuzzi, G.; Sansò, P. Boulders transport by catastrophic waves along the Ionian coast of Apulia (southern Italy). *Mar. Geol.* **2000**, *170*, 93–103. [CrossRef]
26. Sansò, P.; Calcagnile, L.; Fago, P.; Mazzotta, S.; Negri, S.; Quarta, G.; Romagnoli, C.; Vitale, A.; Mastronuzzi, G. Sand Ridges on Rocky Coastal Platforms as Markers of Tsunami Impact: A Multi-Disciplinary Analysis along the Ionian Coast of Southern Apulia (Italy). *Geosciences* **2020**, *10*, 204. [CrossRef]
27. Delle Rose, M.; Fidelibus, C.; Orlanducci, L. Ipotesi sullo spostamento di massi costieri per effetto di onde di bore. *Geol. dell'Ambiente* **2020**, *28*, 21–27. (In Italian)
28. Dai Pra, G. The Late Pleistocene marine deposits of Torre Castiglione (Southern Italy). *Geogr. Fis. Din. Quat.* **1992**, *5*, 115–119.
29. Delle Rose, M.; Federico, A. Karstic phenomena and environmental hazard in the Salento coastal plains (Southern Italy). In Proceedings of 9th International Associate Engineering Geology Congress, Durban, South Africa, 16–20 September 2002; pp. 1297–1305.
30. Morucci, S.; Picone M.; Nardone, G.; Arena, G. Tides and waves in the central Mediterranean Sea. *J. Oper. Oceanogr.* **2016**, *9*, s10–s17. [CrossRef]
31. Dentale, F.; Furcolo, P.; Pugliese Carratelli, E.; Reale, F.; Contestabile, P.; Tomasicchio G.R. Extreme wave analysis by integrating model and wave buoy data. *Water* **2018**, *10*, 373. [CrossRef]
32. GLOBO-BOLAM-MOLOCH Forecast. Available online: Http://www.isac.cnr.it/dinamica/projects/forecasts/index (accessed on 15 November 2019).
33. Trini Castelli, S.; Bisignano, A.; Donateo, A.; Landi, T.C.; Martano, P.; Malguzzi, P. Evaluation of the turbulence parametrization in the MOLOCH meteorological models. *Q. J. R. Meteorol. Soc.* **2019**, *146*, 124–140. [CrossRef]
34. Istituto Superiore Protezione e Ricerca Ambientale: Dinamica e Anomalia Dell'Evento del 12 November 2019 (in Italian). Available online: Http://www.ismar.cnr.it/file/news-e-eventi/Dati (accessed on 4 August 2020).
35. Greece Extreme Weather: Medicane Features, Stormy Winds up to 10 Beaufort. Available online: Https://www.keeptalkinggreece.com/2019/11/11/greece-extreme-weather-medicane-10beaufort-ionian/ (accessed on 29 July 2020).
36. Sistema Informativo Meteo Oceanografico Delle Coste Pugliesi (SIMOP). Available online: Http://93.51.158.171/web/simop/misure (accessed on 16 May 2020).
37. OGIMET Weather Information Service. Available online: Https://www.ogimet.com/home.phtml.en (accessed on 11 December 2019).
38. Owens, E.H. Sea conditions. In *Beaches and Coastal Geology*; Springer: Boston, MA, USA, 1984; p. 722.
39. Hsu, S.A. (Ed.) *Coastal Meteorology*; Academic Press: Cambridge, MA, USA, 1988; pp. 260.
40. Burroughs, L. Wave forecasting by manual methods. In *Guide to Wave Analysis and Forecasting*; World Meteorological Organization, Ed.; Secretariat of World Meteorological Organization: Geneva, Switzerland, 1998; pp. 43–56.
41. Barua, D.K. Wave hindcasting. In *Encyclopedia of Coastal Science*; Finkl, C.W., Makowski, C., Eds.; Springer International Publishing: Berlin/Heidelberg, Germany, 2019; pp. 1859–1864.
42. Knight, J.; Burningham, H. Boulder dynamics on an Atlantic-facing rock coastline, northwest Ireland. *Mar. Geol.* **2011**, *283*, 56–65. [CrossRef]
43. Blott, S.G.; Pye, K. Particle shape: A review and new methods of characterization and classification. *Sedimentology* **2008**, *55*, 31–63. [CrossRef]
44. Nandasena, N.A.K.; Paris, R.; Tanaka, N. Reassessment of hydrodynamic equations: Minimum flow velocity to initiate boulder transport by high energy events (storms, tsunamis). *Mar. Geol.* **2011**, *281*, 70–84. [CrossRef]
45. Imamura, F.; Goto, K.; Ohkubo, S. A numerical model for the transport of a boulder by tsunami. *J. Geophys. Res. Ocean.* **2008**, *113*, C01008. [CrossRef]
46. Engel, M.; May, S.M. Bonaire's boulder fields revisited: Evidence for Holocene tsunami impact on the Leeward Antilles. *Quat. Sci. Rev.* **2012**, *54*, 126–141. [CrossRef]
47. Biolchi, S.; Furlani, S.; Devoto, S.; Scicchitano, G.; Korbar, T.; Vilibic, I.; Sepic, J. The origin and dynamics of coastal boulders in a semi-enclosed shallow basin: A northern Adriatic case study. *Mar. Geol.* **2019**, *411*, 62–77. [CrossRef]
48. Pignatelli, C.; Sansò, P.; Mastronuzzi, G. Evaluation of tsunami flooding using geomorphologic evidence. *Mar. Geol.* **2009**, *260*, 6–18. [CrossRef]
49. Vann Jones, E.C.; Rosser, N.J.; Brain, M.J. Alongshore variability in wave energy transfer to coastal cliff. *Geomorphology* **2018**, *322*, 1–14. [CrossRef]

50. Cox, R.; Ardhuin, F.; Dias, F.; Autret, R.; Beisiegel, N.; Earlie, C.S.; Herterich, J.G.; Kennedy, A.; Paris, R.; Raby, A.; et al. Systematic Review Shows That Work Done by Storm Waves Can Be Misinterpreted as Tsunami-Related Because Commonly Used Hydrodynamic Equations Are Flawed. *Front. Mar. Sci.* **2020**, *7*, 4. [CrossRef]
51. Rovere, A.; Casella, E.; Harris, D.L.; Lorscheid, T.; Nandasena, N.A.K.; Dyer, B.; Sandstrom, M.R.; Stocchi, P.; D'Andrea, W.J.; Raymo, M.E. Giant boulders and Last Interglacial storm intensity in the North Atlantic. *Proc. Natl. Acad. Sci. USA* **2017**, *114*, 12144–12149. [CrossRef] [PubMed]
52. Herterich, J.G.; Dias, F. Potential flow over a submerged rectangular obstacle: Consequences for initiation of boulder motion. *Eur. J. Appl. Math.* **2020**, *31*, 646–681. [CrossRef]
53. Weiss, R.; Diplas, P. Untangling boulder dislodgement in storms and tsunamis: Is it possible with simple theories? *Geochem. Geophys. Geosyst.* **2015**, *16*, 890–898. [CrossRef]
54. Zainali, A.; Weiss, R. Boulder dislodgement and transport by solitary waves: Insights from three-dimensional numerical simulations. *Geophys. Res. Lett.* **2015**, *42*, 4490–4497. [CrossRef]
55. Carbone, F.; Dutykh, D.; Dudley, J.M.; Dias, F. Extreme wave runup on a vertical cliff. *Geophys. Res. Lett.* **2013**, *40*, 3138–3143. [CrossRef]
56. Herterich, J.G.; Cox, R.; Dias. F. How does wave impact generate large boulders? Modeling hydraulic fracture of cliffs and shore platforms. *Mar. Geol.* **2018**, *399*, 34–46. [CrossRef]
57. Hibberd, S.; Peregrine, D.H. Surf and run-up on a beach: A uniform bore. *J. Fluid Mech.* **1979**, *95*, 323–345. [CrossRef]
58. Cox, J.C.; Machemehl, J. Overload bore propagation due to an overtopping wave. *J. Waterw. Port Coast. Ocean Eng.* **1986**, *112*, 161–163. [CrossRef]
59. Whittaker, C.N.; Fitzgerald, C.J.; Raby, A.C.; Taylor, P.H.; Borthwick, A.G.L. Extreme coastal responses using focused weve groups: Overtopping and horizontal forces exerted on an inclined seawall. *Coast. Eng.* **2018**, *140*, 292–305. [CrossRef]
60. Ryu, Y.; Chang, K.; Mercier, R. Runup and green water velocities due to breaking wave impinging and overtopping. *Exp. Fluids* **2007**, *43*, 555–567. [CrossRef]
61. Roeber, V.; Bricker, J.D. Destructive tsunami-like wave generated by surf beat over a coral reef during Typhoon Haiyan. *Nat. Commun.* **2015**, *6*, 7854. [CrossRef]
62. Cox, R.; Jahn, K.L.; Watkins. O.G.; Cox, P. Extraordinary boulder transport by storm waves (west of Ireland, winter 2013–2014), and criteria for analysing coastal boulder deposits. *Earth Sci. Rev.* **2018**, *177*, 623–636. [CrossRef]
63. Paris, R.; Naylor, L.A.; Stephenson, W.J.S. Boulders as a signature of storms on rock coasts. *Mar. Geol.* **2011**, *283*, 1–11. [CrossRef]
64. Sunamura T. Rocky coast processes: With special reference to the recession of soft rock cliffs. *Proc. Jpn. Acad. Ser. B* **2015**, *91*, 481–500. [CrossRef]
65. Wolters, G.; Muller, G. The propagation of wave impact induced pressures into cracks and fissure. *Geol. Soc. Lond. Eng. Geol. Spec. Publ.* **2004**, *20*, 121–130. [CrossRef]


**Sample Availability:** Photograph survey documentation is available from M.D.R.